

Boosting Edge Detection with Pixel-wise Feature Selection: The Extractor-Selector Paradigm

Hao Shu*

* Sun-Yat-Sen University, Shenzhen, China.

* Shenzhen University, Shenzhen, China.

Abstract—Deep learning has significantly advanced image edge detection (ED), primarily through improved feature extraction. However, most existing ED models apply uniform feature fusion across all pixels, ignoring critical differences between regions such as edges and textures. To address this limitation, we propose the Extractor-Selector (E-S) paradigm, a novel framework that introduces pixel-wise feature selection for more adaptive and precise fusion. Unlike conventional image-level fusion that applies the same convolutional kernel to all pixels, our approach dynamically selects relevant features at each pixel, enabling more refined edge predictions. The E-S framework can be seamlessly integrated with existing ED models without architectural changes, delivering substantial performance gains. It can also be combined with enhanced feature extractors for further accuracy improvements. Extensive experiments across multiple benchmarks confirm that our method consistently outperforms baseline ED models. For instance, on the BIPED2 dataset, the proposed framework can achieve over 7% improvements in ODS and OIS, and 22% improvements in AP, demonstrating its effectiveness and superiority.

I. INTRODUCTION

Image edge detection (ED) is a fundamental task in computer vision, supporting a wide range of high-level applications such as image inpainting[1], object detection[2], and image segmentation[3]. Early approaches, including the Sobel operator[4] and the Canny algorithm[5], utilized gradient-based criteria to develop effective edge detectors. Subsequently, statistical methods with hand-crafted features were proposed[6, 7] to enhance performance. With the maturation of machine learning research, learning-based algorithms have gained significant traction[8–13]. In particular, convolutional neural network (CNN)-based models have rapidly established themselves as state-of-the-art (SOTA) approaches[14–17], owing to their strong feature extraction capabilities. Notable examples such as Holistically-Nested Edge Detection (HED)[18], Bi-Directional Cascade Network (BDCN)[19], and Dense Extreme Inception Network (Dexi)[20] have demonstrated impressive performance by effectively handling complex edge structures. More recently, transformer-based[21, 22] and diffusion-based[23, 24] architectures have also been explored, though they remain less mature than their CNN-based counterparts.

A well-performing ED model should exhibit several critical properties. First, it must achieve high precision on established benchmarks, providing numerical validation of its effectiveness. Second, it should produce perceptually accurate results.

Third, and importantly, it should perform well without relying on post-processing techniques such as non-maximum suppression (NMS), which are non-differentiable and hinder end-to-end optimization in downstream tasks.

A challenge in ED lies in the inherent ambiguity of defining edges, making it difficult to devise reliable hand-crafted detection criteria. For instance, classical methods like the Canny algorithm[5] rely on gradient features, but textural regions can also exhibit strong gradients despite not corresponding to true edges. This ambiguity demonstrates the importance of comprehensive feature-extracting schemes and necessitates learning-based approaches that extract various cues from annotated datasets. Consequently, CNN-based models[15, 18–20, 25] have become dominant in this context due to their superior feature extraction capabilities.

However, despite their strengths in feature extraction, most CNN-based ED models underexplore the importance of feature fusion. These models typically extract multi-scale features using tens of millions of parameters, yet fuse them using overly simplistic mechanisms—often a single 1×1 convolution layer. This uniform fusion does not distinguish between edge and non-edge pixels. Still, in reality, effective feature fusion should be pixel-adaptive: edge pixels benefit from high-resolution features for precise delineation, while texture pixels should emphasize low-level features for suppression purposes. As a result, the indiscriminate fusion currently employed leads to suboptimal predictions. If the feature fusion could be more diverse and context-aware, detection performance would likely improve.

Motivated by this observation, we propose a novel feature **Extractor-Selector (E-S)** paradigm to enhance ED through a pixel-wise feature selection mechanism. This paradigm enables adaptive fusion tailored to individual pixels, treating edge and texture regions differently—unlike traditional uniform fusion schemes that fuse all pixels via the same convolutional kernel. The E-S framework consists of two key components: a multi-scale feature extractor that provides diverse feature representations, and a pixel-wise selector that learns to weight these features appropriately. To ensure compatibility with existing ED architectures, the extractor adopts existing CNN-based models, leveraging their proven strengths, while the selector is newly designed as an independent module since no existing model is available. Integration is seamless—existing extractors can be used without modification or with minimal adaptation, yielding significant performance gains either way. Through this pixel-level selection, our approach significantly

enhances the accuracy and perceptual quality of edge predictions, as validated by comprehensive experiments.

Our main contributions can be summarized as follows:

- We identify a fundamental limitation in the uniform feature fusion mechanisms used by previous ED models and address it by introducing the Extractor-Selector (E-S) paradigm.
- We propose a pixel-wise feature selector and seamlessly integrate it with existing ED models that serve as feature extractors. The resulting E-S framework achieves state-of-the-art performance.
- We further enhance the E-S framework by modifying extractors to support richer feature selection and mitigate information loss, leading to additional improvements in prediction quality. The enhanced version of the E-S framework is called the **EES** framework.
- We conduct extensive experiments on multiple benchmark datasets, demonstrating consistent improvements over models without the E-S framework, highlighting its effectiveness and superiority.
- We show that the improvements stem from the E-S paradigm itself, rather than from specific choices of the selector architecture, underscoring the general applicability and robustness of our approach.

II. PREVIOUS WORKS

This section reviews related works relevant to the study.

A. Datasets

In the early stages of ED research, the task was often conflated with related problems such as contour detection, boundary detection, and segmentation. As a result, early studies typically employed datasets that were not specifically designed for ED but adapted from other tasks. A notable example is the Berkeley Segmentation Dataset BSDS300 and its extended version BSDS500[26], which contain 300 and 500 RGB images, respectively, annotated with contours by multiple human annotators. These datasets are primarily used for contour detection today. Similarly, the Multi-cue Boundary Dataset (MDBD)[27] provides 100 high-resolution images annotated with boundary information across diverse scenes and is commonly used for boundary detection. The NYU Depth Dataset (NYUD) and its extension NYUD2[28] offer hundreds of thousands of RGB-D indoor scene images, including 1,449 images labeled for segmentation. Other commonly used datasets include PASCAL VOC[29], Microsoft COCO[30], SceneParse150[31], and Cityscapes[32]. While these datasets have significantly contributed to the advancement of ED, their primary focus on other vision tasks limits their specificity and suitability for modern ED research.

As ED evolved into a distinct research field, specialized datasets were introduced to address its unique requirements. The BIPED dataset, later refined into BIPED2[33], contains 250 high-resolution images with single-edge annotations. The BRIND dataset[34] re-annotates BSDS500 by categorizing edges into four types: reflectance, illumination, normal, and depth. The UDED dataset[35], introduced in 2023, consists

of 29 carefully selected images with high-quality edge annotations, further enriching the ED benchmark suite, though its limited scale constrains its broader applicability.

A persistent challenge across ED datasets is their reliance on human annotations for ground truth labeling. These annotations are inherently noisy, often including missing edges, errors, or inconsistencies. Annotation uncertainty also arises when different annotators produce divergent results for the same image—or even when the same annotator produces different annotations at different times. To address these challenges, recent efforts have focused on improving annotation quality using advanced labeling techniques and developing models that are robust to noisy annotations[36–38].

B. Models

The development of ED methodologies can be broadly divided into three phases: heuristic-based methods, statistical approaches, and deep learning-based models.

Heuristic-Based Methods: Early ED methods employed simple heuristic criteria, such as intensity gradients, to design efficient edge detectors. Classical techniques such as the Sobel operator[4] and the Canny detector[5] remain widely known due to their simplicity and effectiveness. However, these methods exhibit limited adaptability to complex datasets, as their fixed coefficients struggle to distinguish true edges from textures in diverse scenes.

Statistical and Early Learning-Based Methods: The second phase introduced statistical and early learning-based techniques that improved performance using hand-crafted features. These included Chernoff information[6], histograms[7], textures[8], and sketch tokens[11]. Methods such as structured forests[13], nearest-neighbor search[12], and logistic regression[10] were used to classify pixels or patches as edge or non-edge. These approaches offered improved accuracy and robustness over heuristic methods, but their reliance on manual feature design limited scalability and generalization to more complex datasets. Consequently, they were gradually outpaced by deep learning approaches.

Deep Learning-Based Methods: The third and current phase is dominated by deep learning, particularly convolutional neural networks (CNNs). CNN-based ED models have revolutionized the field by enabling hierarchical feature extraction and end-to-end learning. Holistically-Nested Edge Detection (HED)[18] introduced multi-scale learning by fusing features from different scales to enhance edge prediction. Richer Convolutional Features (RCF)[15] extended this by aggregating features from multiple stages within the same layer. Bi-Directional Cascade Networks (BDCN)[19] and Pixel Difference Networks (PiDiNet)[17] introduced novel architectures to improve edge precision. RINDNet[34] addressed multiple edge types through multi-stage fusion, while DexiNet[20] leveraged dense skip connections for better accuracy. More recently, transformer-based[21, 22] and diffusion-based[23, 24] models have emerged, offering promising alternative paradigms, though they are still less mature than CNN-based methods.

C. Loss Functions

Most ED models rely on weighted binary cross-entropy (WBCE) loss, which promotes high precision but struggles to produce crisp, thin edges without post-processing techniques such as non-maximum suppression (NMS). To overcome this limitation, alternative loss functions such as Dice loss[39] and tracing loss[40] have been proposed to produce thinner edges. However, these often involve trade-offs in precision or require careful hyperparameter tuning across datasets and models. Another key issue is the class imbalance between edge and non-edge pixels, which can degrade model performance. In response, methods such as AP-loss[41] and Rank-loss[42] have been introduced. However, the WBCE loss is still the most popular one currently.

D. Encoder-Decoder Framework in Transformers

Originally developed for natural language processing[43], the encoder-decoder framework has proven effective for image processing tasks as well[44]. This structure captures long-range dependencies without necessitating excessively deep architectures, in contrast to traditional CNNs. Transformer-based models leveraging this framework have shown success in tasks such as object detection[45], semantic segmentation[46], and image super-resolution[47]. Recently, transformers have also been applied to contour detection[21], expanding their utility within the ED domain.

E. Evaluation Benchmarks

The most widely adopted evaluation protocol for ED follows the methodology proposed in [8], using three standard metrics:

- **Optimal Dataset Score (ODS):** Measures the best F-score across the entire dataset.
- **Optimal Image Score (OIS):** Computes the best F-score per image, then averages the scores.
- **Average Precision (AP):** Evaluates the mean precision-recall performance.

These metrics are computed under a predefined error tolerance distance, which allows slight misalignments between predicted and ground-truth edges. However, the choice of error tolerance often varies across datasets and studies due to reliance on default parameters. Limited attention has been given to standardizing this parameter until a recent study analyzed its effect and advocated for a 1-pixel tolerance to provide the most rigorous evaluation benchmark[38].

III. METHODOLOGY

This section presents our proposed approach. We will begin by analyzing the limitations in existing ED models. Then, we will introduce the standard Extractor-Selector (E-S) paradigm and a selector model for achieving it, followed by an enhanced version—the Enhanced E-S (EES) framework—designed to improve feature quality and reduce information loss to further improve the final edge predictions. Finally, we will describe the training strategies used for the proposed schemes.

A. The challenge in Existing Models

Conventional ED models can be divided into two stages: feature extraction and feature fusion. While significant effort is dedicated to building powerful extractors—often comprising tens of millions of parameters—the feature fusion step is often overly simplistic, commonly implemented as a single 1×1 convolution layer. This imbalance limits the models’ ability to leverage the rich multi-scale features extracted in the first stage.

Essentially, feature fusion in ED is inherently a feature selection problem. Effective edge detection requires high-resolution features for localizing edge pixels precisely and low-resolution features for suppressing texture noise in non-edge regions. However, a 1×1 convolution layer applies the same weights across all spatial locations, failing to distinguish between edge and non-edge regions. Consequently:

- If high-resolution features are prioritized by the fusion layer, texture regions may be misclassified as edges (false positives).
- If low-resolution features are prioritized by the fusion layer, edges may become blurry or inaccurate (false negatives).

Thus, even with globally optimized weights, this uniform treatment limits the model’s ability to perform well across all pixel types.

As demonstrated in [38], enhancing the fusion process yields performance gains. However, simply stacking additional convolutional layers as in the paper only marginally alleviates the issue because it fails to resolve the underlying problems stated above. The limited capacity of shallow convolutional fusion modules is insufficient to fully exploit the rich feature sets produced by modern extractors, nor to provide differentiated feature selections between edge and texture pixels.

This motivates the introduction of a dedicated feature selection module capable of assigning pixel-wise adaptive weights to multi-scale features—allowing for more discriminative and precise feature selection for edge predictions.

B. The Standard E-S Architecture

To address the above challenge, we propose the E-S framework. It preserves traditional ED models as feature extractors but introduces a dedicated feature selector that assigns pixel-wise weights to multi-scale features for selecting the extracted features, thereby enhancing both accuracy and perceptual quality.

The E-S framework consists of two components: a feature extractor that captures multi-scale features from input images, and a feature selector that assigns pixel-wise weights to extracted features to generate refined edge maps. An overview of the framework is shown in Figure 1.

The extractor can adopt any existing high-performance ED model—such as HED[18], BDCN[19], Dexi[20], or even their combination, to leverage their superior feature extraction capabilities. However, because no off-the-shelf selector model exists, a custom selector architecture is required, which will be introduced in the next subsection.

Generally, the E-S framework can be formulated as:

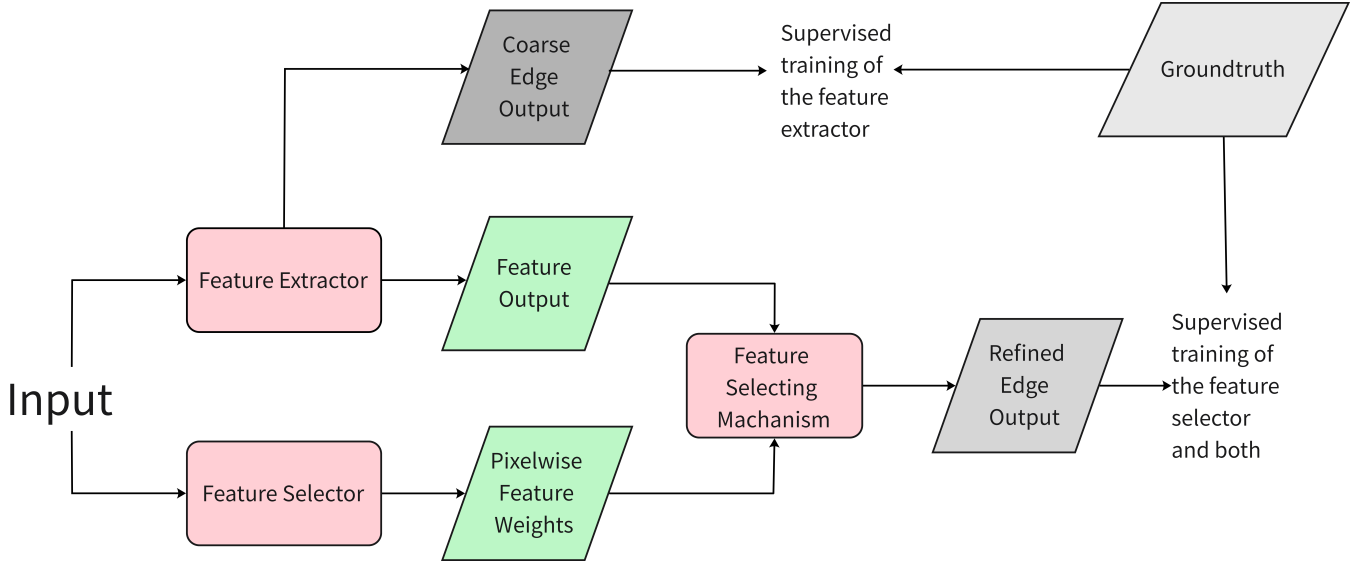


Fig. 1 The framework of the E-S paradigm. It consists of two components: a feature extractor which produces features and coarse edge maps, and a feature selector which selects the features for refinements. The combination of the two components ultimately outputs the final edge predictions.

$$Edge(I) = FSM(P_2(E_\theta(I)), S_\eta(I)) \quad (1)$$

$$FSM : \mathbb{R}^{C \times H \times W} \times \mathbb{R}^{C \times H \times W} \rightarrow \mathbb{R}^{1 \times H \times W} \\ (A, B) \mapsto \sum_{dim: 1} (A \odot B) \quad (2)$$

$$E_\theta : \mathbb{R}^{3 \times H \times W} \rightarrow \mathbb{O} \times \mathbb{R}^{C \times H \times W} \\ I \mapsto (P_1(E_\theta(I)), P_2(E_\theta(I))) \quad (3)$$

$$S_\eta : \mathbb{R}^{3 \times H \times W} \rightarrow \mathbb{R}^{C \times H \times W} \\ I \mapsto S_\eta(I) \quad (4)$$

where P_1 and P_2 denote the projections onto the first and second components of a direct product, respectively. I represents the input image. The symbol \odot denotes point-wise multiplication, and $\sum_{dim:1}$ denotes summation over the first dimension (i.e. the channel dimension). The functions E_θ and S_η refer to the networks of the feature extractor and feature selector, respectively, parameterized by θ and η , both outputting C channels from an input 3-channel (RGB) image. \mathbb{O} represents the space of edge maps produced by the extractor, while the second output component of E_θ corresponds to its outputted feature. Here, H and W are the height and width of the input image.

In the standard implementation, the selector assigns pixel-wise weights directly to the final multi-scale feature maps outputted by the extractor to produce the final edge prediction. Thus, $P_1(E_\theta(I))$ corresponds to the extractor's original edge map outputs, typically as a list, while $P_2(E_\theta(I))$ is their concatenation. Moreover, a slight modification to the extractor can further enhance performance, where $P_1(E_\theta(I))$ and $P_2(E_\theta(I))$ are significantly different. This improved design will be discussed in detail two sections later.

C. Design of the Feature Selector

The selector should be selected with some key properties, including high expressive capacity to enable diverse and precise feature selection and adequate degrees of freedom to generate pixel-wise adaptive weights. Since these properties align with established deep learning paradigms, we employ a deep U-Net-inspired architecture for adequate degrees of freedom and combine CNNs with transformer encoders for high expressive capacity. CNNs excel at capturing short-range dependencies, which are crucial for local edge refinement, while transformers effectively model long-range dependencies using a relatively shallow structure. Combining these architectures ensures both local precision and global consistency and therefore enriches the expressive capacity of the architecture.

An overview of the selector structure is shown in Figure 2. It follows a U-Net-like CNN backbone, and at the $\frac{1}{8}$ and $\frac{1}{16}$ scales, transformer-based encoder-decoder structures are integrated. The final fusion stage employs a three-layer architecture, similar to SDPED[38], which has been proven to be effective. Additionally, trainable coefficients are added to the residual connections to optimize the balance between the output features and those linked through the residual connections.

D. The EES Architecture

While the standard E-S framework enables pixel-wise selection, it only operates on the final fused outputs from the extractor. These features, having passed through several compression layers, often lose valuable detail. Inspired by RCF[15], which enriches feature utilization in HED[18], we propose an Enhanced framework, namely the EES framework, that exposes the selector to richer, less compressed features from earlier stages of the extractor.

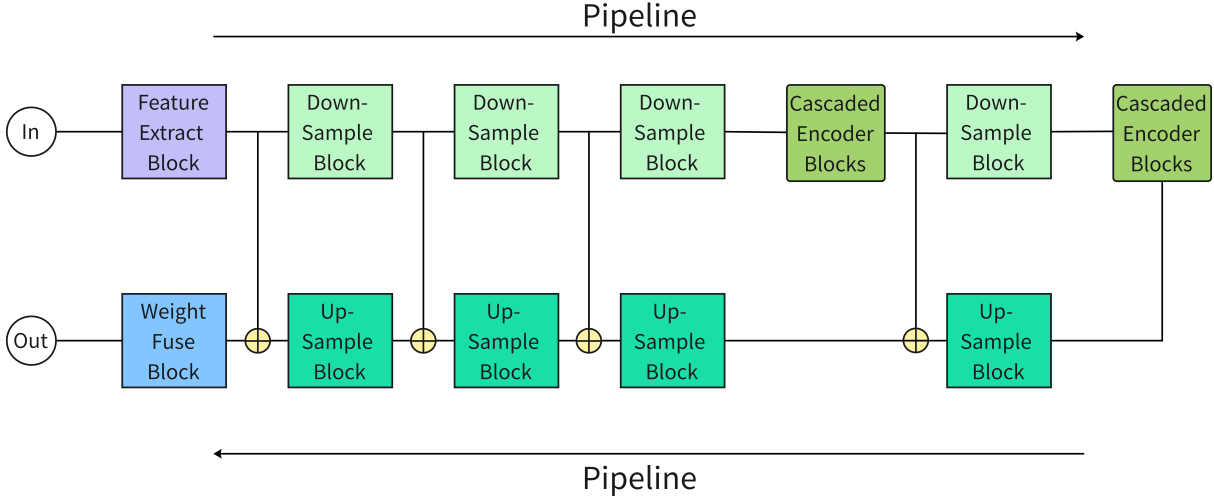


Fig. 2 An overview of the feature selector architecture: It is structured like a U-Net. The input images pass through a feature extraction block, followed by four $\frac{1}{2}$ down-sampling blocks to capture multi-scale features. At the $\frac{1}{8}$ and $\frac{1}{16}$ scales, cascaded transformer encoder blocks are applied. The features from the $\frac{1}{16}$ scale are progressively up-sampled, and each up-sample block incorporates a residual connection with a learnable coefficient to balance the up-sampled features and the features from the residual connections. Finally, pixel-wise weights are produced by fusing the ordinary-scale features. Detailed block designs are presented in supplementary materials.

To this end, we modify the extractor’s fusion and upsampling modules, without altering its backbone, as shown in Figures 3 and 4.

Specifically, previous ED models (Figure 3), which serve as extractors in the E-S framework, typically consist of a backbone network with down-sampling blocks that progressively reduce the spatial resolution. Multi-scale features are then obtained, fused to one or two edge maps in each scale, and passed through up-sampling blocks to generate final features, at the target resolution, which are further fused to produce the final edge map. Although this structure has been effective in many cases, the final features often suffer from significant information loss and lack of diversity due to the compressed fusion schemes before up-sampling.

In contrast, the modified architecture (Figure 4) integrates multi-scale features into a suitable number of channels, which are then up-sampled without fusion. The up-sampled features are used as the output, offering richer information with reduced loss for selection. Although the final outputted features are still fused into coarse edge maps for pre-training the extractor, it is the unfused features that are used by the selector for the final predictions. Additionally, we introduce two fixed feature maps (one of zeros and one of ones) to assist the selector in making more confident decisions, particularly in cases where a pixel is strongly classified as belonging to either the edge or non-edge region.

E. Training Strategy

A three-stage training strategy is adopted:

- Stage 1 (Feature Extractor Pretraining): The feature extractor is trained independently via its edge outputs $P_1(E_\theta(I))$, using its default loss function L_E . Namely,

$$\theta_E = \arg \min_{\theta^*} L_E(P_1(E_\theta(I)), Label(I)) \quad (5)$$

where $Label(I)$ denotes the ground-truth of the input image I .

- Stage 2 (Feature Selector Training): The feature extractor’s parameters are frozen while the feature selector is trained separately using loss function L_S , typically the WBCE loss. Namely,

$$\eta_S = \arg \min_{\eta^*} L_S(FSM(P_2(E_{\theta_E}(I), S_{\eta^*}(I))), Label(I)) \quad (6)$$

- Stage 3 (Union Tuning): Both the feature extractor and selector are trained jointly with loss function L_U , typically WBCE. Namely,

$$\theta, \eta = \arg \min_{\theta^*, \eta^*} L_U(FSM(P_2(E_{\theta^*}(I), S_{\eta^*}(I))), Label(I)) \quad (7)$$

where the initial θ^* and η^* are set to θ_E and η_S , respectively.

The WBCE loss is defined as:

$$L_{WBCE}(\hat{Y}, Y) = \alpha \sum_{y_i \in Y^+} \log(\hat{y}_i) - \lambda(1 - \alpha) \sum_{y_i \in Y^-} \log(1 - \hat{y}_i) \quad (8)$$

where:

- \hat{y}_i is the pixel in the prediction \hat{Y} corresponding to y_i .
- Y^+ represents the set of edge pixels in the ground-truth Y (positive samples).
- Y^- denotes the set of non-edge pixels in the ground-truth (negative samples).
- $\alpha = \frac{|Y^-|}{|Y|}$ is the weight balancing the positive and negative samples.
- $\lambda = 1.1$ as suggested in previous works.

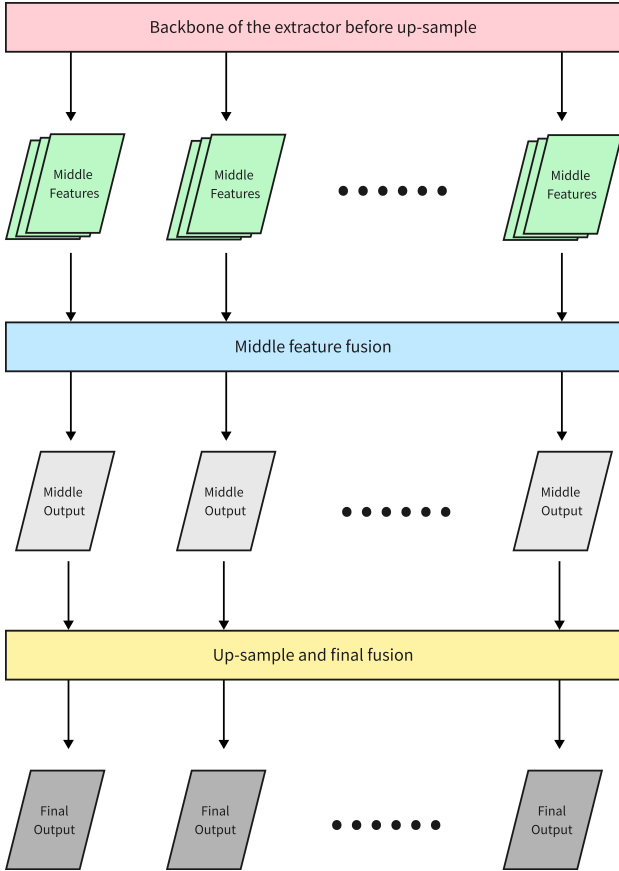


Fig. 3 The standard extractor architecture: The backbone network extracts multi-scale features through progressive down-sampling. These features are then fused into one or two edge maps at each scale and then up-sampled to the original image resolution. The final edge prediction is obtained by fusing these up-sampled maps. However, because the features are compressed prior to up-sampling, the resulting high-resolution representations often suffer from substantial information loss, limiting the usage by the selector.

IV. EXPERIMENT

This section presents our experimental setup, results, and ablation studies to validate the effectiveness of the proposed frameworks.

A. Experimental Setup and Benchmarks

The experimental setup follows the methodology outlined in [8] and refined in [38]. Below, we provide detailed descriptions of the datasets, augmentation techniques, training procedures, and evaluation criteria.

1) *Datasets and Data Augmentation:* The main experiments are conducted on three ED datasets: BRIND[34], UDED[35], and BIPED2[33]. Additional experiments are available in the supplementary material. The preprocessing of the dataset is stated as follows.

Label employments:

- For BRIND, all annotated edge maps are merged into a single binary ground truth map per image. A pixel is marked as an edge if any annotator labeled it as such.
- UDED and BIPED2 provide single, unique ground truth edge annotations per image, which are used directly.

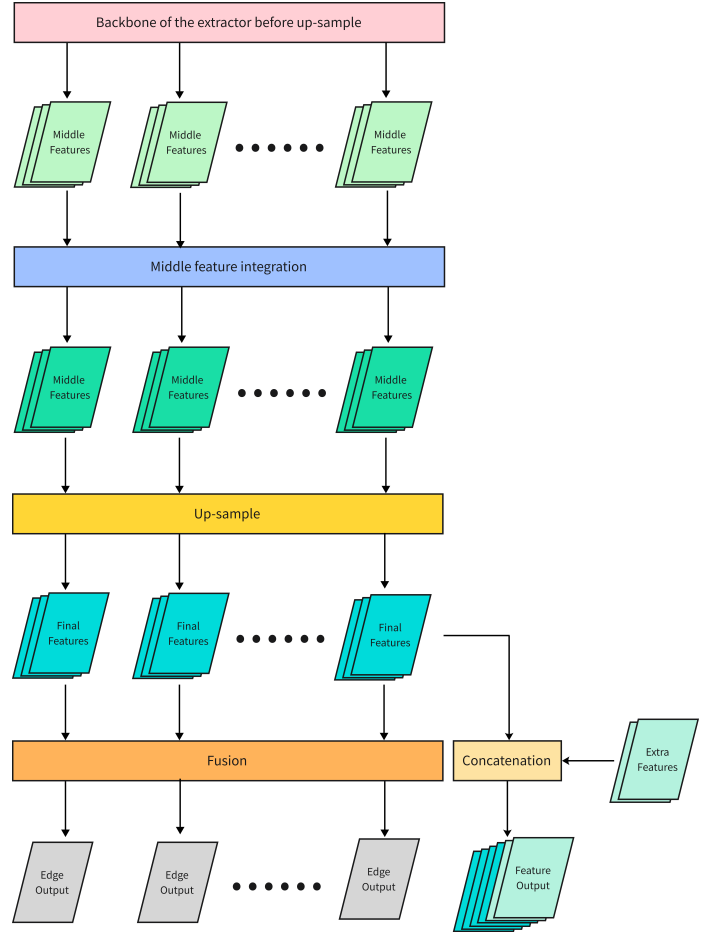


Fig. 4 The modified feature extractor architecture. Unlike the standard extractor architecture, which compresses multi-scale features before up-sampling, the modified version preserves richer information by avoiding early fusion. It uses the same backbone to extract multi-scale features, which are first unified to a suitable number of channels and then up-sampled without compression. Two additional fixed feature maps (one filled with zeros and one with ones) are appended to assist the selector in identifying highly confident edge and non-edge regions. Although a coarse fusion is applied during pre-training of the extractor, it is these enhanced, unfused features that are passed to the selector for final prediction, providing more refined and less lossy representations compared to the standard approach.

Dataset splits:

- BRIND: 500 images, split into 400 training and 100 test samples.
- BIPED2: 250 images, split into 200 training and 50 test samples.
- UDED: 27 usable images (after excluding two with height or width lower than 320 pixels), split into 20 training and 7 test samples.

Data augmentation (follows [38]):

- Each image is recursively split in half until its height and width are both lower than 640 pixels.
- Augmentation includes rotations (0° , 90° , 180° , and 270°) and horizontal flips.
- Noiseless data are added.

2) *Training Notes:* During training, 320×320 pixel crops are sampled randomly and refreshed every 5 epochs. All

models are optimized using Adam with a learning rate of 10^{-4} , weight decay of 10^{-8} , and batch size of 8. The training procedure is stated as follows.

Training process:

- Stage 1 (Feature Extractor Pretraining): The extractor is trained independently, with 50 epochs for the BRIND and BIPED2, and 200 epochs for the UDED, respectively.
- Stage 2 (Feature Selector Training): The selector is trained, freezing the extractor parameters, with an additional 50 epochs for BRIND and BIPED2, and 200 epochs for UDED, respectively.
- Stage 3 (Union Stage): Both the extractor and the selector are trained jointly, with another 50 epochs for BRIND and BIPED2, and 200 epochs for UDED, respectively.

3) *Evaluation Metrics*: Performance is evaluated using the framework from [8], with a strict 1-pixel error tolerance as suggested in [38]. This is in contrast to most prior works which used error tolerances of 4 to 11 pixels, and the reason for using 1-pixel error tolerance has been discussed in [38]¹. All results are reported without post-processing, such as non-maximum suppression, whose reason has been illustrated in the introduction. Results with traditional relaxed error tolerances with post-processing are provided in the supplementary material. To assess the effectiveness of the proposed frameworks:

We evaluate:

- The original extractor models (previous models), including HED[18], BDCN[19], and Dexi[20]). They serve as baseline models.
- The corresponding E-S versions (of each baseline model) without joint training (denoted -ES).
- The corresponding E-S versions with joint training (denoted -ES-U).
- The corresponding EES versions without joint training (denoted -EES).
- The corresponding EES versions with joint training (denoted -EES-U).

For fairness:

- All models are trained or re-trained under identical settings given above.
- All models are trained with WBCE loss, which was also used as the default loss function of the baseline models.
- All results undergo the same prediction Procedure: Test images are processed in overlapping 320×320 patches with 16-pixel overlap.² Overlapping regions are averaged to ensure spatial consistency in the final output.

B. Experiment Results

Results for the BIPED2, BRIND, and UDED datasets (under 1-pixel error tolerance and without NMS) are summarized in Tables I, II, and III, respectively. They include the performance of various feature extractors and their combinations with

¹The 1-pixel error tolerance corresponds to setting the error toleration distance to 0.001 for BIPED2 and 0.003 for BRIND and UDED in the MATLAB evaluation code from [8].

²If the last patch in a row or column is smaller than 304 pixels, additional overlap is applied to the last two patches in that row or column to ensure the last patch is of 320×320 . Details can be found in the implementation codes.

feature selectors, both the standard and the enhanced versions. The improvements relative to the baseline models are explicitly indicated.

Quantitative Analysis

In all the benchmark datasets and all the assessing criteria, both the EES and the standard E-S architectures achieve significant improvements. The average improvements over the three extractors, compared to the baseline models, in ODS, OIS, and AP, respectively, are summarized as follows.

For BIPED2:

- Standard E-S framework without union training improves: 3.72%, 3.53%, and 8.00%, respectively.
- Standard E-S framework with union training improves: 6.02%, 6.09%, and 20.00%, respectively.
- EES framework without union training improves: 7.28%, 7.05%, and 22.00%, respectively.
- EES framework with union training improves: 5.83%, 5.93%, and 18.00%, respectively.

For UDED:

- Standard E-S framework without union training improves: 1.95%, 1.60%, and 4.07%, respectively.
- Standard E-S framework with union training improves: 4.60%, 3.07%, and 14.63%, respectively.
- EES framework without union training improves: 5.43%, 4.01%, and 20.19%, respectively.
- EES framework with union training improves: 6.55%, 4.94%, and 13.52%, respectively.

For BRIND:

- Standard E-S framework without union training improves: 1.83%, 1.20%, and 5.51%, respectively.
- Standard E-S framework with union training improves: 1.83%, 1.35%, and 17.40%, respectively.
- EES framework without union training improves: 3.50%, 3.15%, and 10.35%, respectively.
- EES framework with union training improves: 1.83%, 1.20%, and 17.40%, respectively.

These results clearly demonstrate that both the standard E-S and the enhanced EES frameworks significantly improve edge detection performance across all datasets, and EES mostly obtains more gains, which should be attributed to its richer feature representations.

Qualitative Analysis

Figure 5 presents visual comparisons of the predicted results. It showcases full images alongside cropped regions (the blue and yellow boxes). The columns represent the original images, ground-truths, and the predictions, respectively. Notably, the proposed EES architecture generates more perceptual edge predictions compared to the baseline model.

C. Ablation studies

We conduct ablation studies to investigate the impact of different selector structures, positional encoding methods in transformer encoder blocks, and the effect of using multiple extractors and selectors. These experiments further validate that the E-S framework itself is the primary contributor to performance improvements.

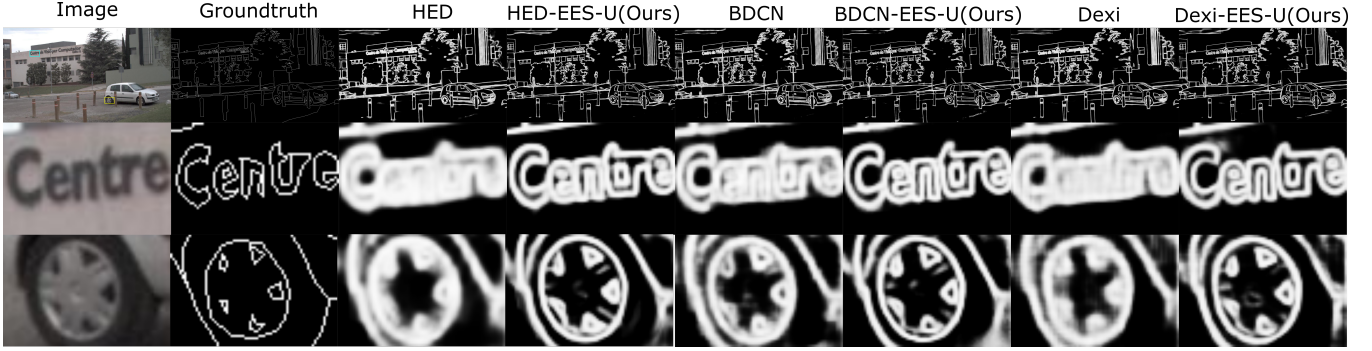


Fig. 5 Visual comparisons of the models: Columns 1 presents the ordinary image and its cropped regions marked by blue (the up-left words) and yellow boxes (the down-right tire), respectively. Column 2 displays the corresponding ground-truths. Columns 3, 5, and 7 display the predictions of the baseline models, while columns 4, 6, and 8 exhibit the predictions of the corresponding EES frameworks. Obviously, the EES frameworks obtain better perceptual results.

TABLE I

Results on BIPED2 with 1-pixel error tolerance without NMS: For each extractor, the first row presents the results of the baseline model, the rows *-ES*, *-ES-U*, *-EES*, and *-EES-U* exhibits results with our frameworks, following the notations in the main-text. The best score among the configurations for each extractor is highlighted in **bold**. Improvements related to the baseline models are indicated in parentheses. The last five rows (A) report average improvements across the three baseline models. Improvements are also indicated in parentheses with the best scores in **bold**.

	BIPED2 with 1-pixel error tolerance without NMS		
	ODS	OIS	AP
HED	0.592	0.602	0.347
HED-ES	0.649 (+9.63%)	0.654 (+8.64%)	0.433 (+24.78%)
HED-EES	0.666 (+12.50%)	0.671 (+11.46%)	0.493 (+42.07%)
HED-ES-U	0.655 (+10.64%)	0.663 (+10.13%)	0.491 (+41.50%)
HED-EES-U	0.659 (+11.32%)	0.665 (+10.45%)	0.490 (+41.21%)
BDCN	0.629	0.635	0.421
BDCN-ES	0.633 (+0.64%)	0.639 (+0.63%)	0.423 (+0.46%)
BDCN-EES	0.652 (+3.66%)	0.655 (+3.15%)	0.473 (+12.35%)
BDCN-ES-U	0.661 (+5.09%)	0.666 (+4.88%)	0.484 (+14.96%)
BDCN-EES-U	0.652 (+3.66%)	0.660 (+3.94%)	0.462 (+9.74%)
Dexi	0.632	0.636	0.432
Dexi-ES	0.640 (+1.27%)	0.644 (+1.26%)	0.441 (+2.08%)
Dexi-EES	0.672 (+6.33%)	0.677 (+6.45%)	0.499 (+15.51%)
Dexi-ES-U	0.650 (+2.89%)	0.656 (+3.14%)	0.465 (+7.64%)
Dexi-EES-U	0.651 (+3.01%)	0.657 (+2.99%)	0.463 (+7.18%)
A	0.618	0.624	0.400
A-ES	0.641 (+3.72%)	0.646 (+3.53%)	0.432 (+8.00%)
A-EES	0.663 (+7.28%)	0.668 (+7.05%)	0.488 (+22.00%)
A-ES-U	0.655 (+6.02%)	0.662 (+6.09%)	0.480 (+20.00%)
A-EES-U	0.654 (+5.83%)	0.661 (+5.93%)	0.472 (+18.00%)

1) *Effect of Positional Encoding:* Table IV presents the performance of the standard E-S architecture with various positional encoding strategies applied to the selector. Two types are examined:

- Standard positional encoding as in [43].
- Rotary positional encoding as in [48]

We test both applying positional encoding to all encoder blocks and only the first encoder block of each level. How-

TABLE II

Results on UDED with 1-pixel error tolerance (for the lowest-resolution images) without NMS: The table is structured as Table I, with results for the UDED dataset.

	UDED without NMS		
	ODS	OIS	AP
HED	0.716	0.751	0.489
HED-ES	0.733 (+2.37%)	0.764 (+1.73%)	0.521 (+6.54%)
HED-EES	0.738 (+3.07%)	0.765 (+1.86%)	0.635 (+29.86%)
HED-ES-U	0.723 (+0.98%)	0.751 (+0.00%)	0.602 (+23.11%)
HED-EES-U	0.754 (+5.31%)	0.782 (+4.13%)	0.616 (+25.97%)
BDCN	0.706	0.744	0.530
BDCN-ES	0.727 (+2.97%)	0.764 (+2.69%)	0.569 (+7.36%)
BDCN-EES	0.750 (+6.23%)	0.777 (+4.44%)	0.628 (+18.49%)
BDCN-ES-U	0.758 (+7.37%)	0.778 (+4.57%)	0.625 (+17.92%)
BDCN-EES-U	0.762 (+7.93%)	0.778 (+4.57%)	0.623 (+17.55%)
Dexi	0.733	0.752	0.600
Dexi-ES	0.737 (+0.55%)	0.759 (+0.93%)	0.598 (-0.33%)
Dexi-EES	0.784 (+6.96%)	0.796 (+5.85%)	0.683 (+13.83%)
Dexi-ES-U	0.771 (+5.18%)	0.786 (+4.52%)	0.629 (+4.83%)
Dexi-EES-U	0.780 (+6.41%)	0.797 (+5.98%)	0.601 (+0.17%)
A	0.718	0.749	0.540
A-ES	0.732 (+1.95%)	0.761 (+1.60%)	0.562 (+4.07%)
A-EES	0.757 (+5.43%)	0.779 (+4.01%)	0.649 (+20.19%)
A-ES-U	0.751 (+4.60%)	0.772 (+3.07%)	0.619 (+14.63%)
A-EES-U	0.765 (+6.55%)	0.786 (+4.94%)	0.613 (+13.52%)

ever, the results indicate that positional encoding provides no observed improvement, suggesting that positional information has already been well captured through the CNN backbone of the selector structure. Similar experiments are also implemented on the EES framework, which exhibit consistent results, please refer to the supplementary materials.

2) *Selector Architecture Variants:* Table V evaluates the effect of different selector designs within the standard E-S architecture.

We test several variants:

- T0: No transformer encoder blocks are employed.
- T1: Encoder blocks only applied at the $\frac{1}{16}$ scale.
- T2: Encoder blocks applied at both $\frac{1}{8}$ and $\frac{1}{16}$ scales,

TABLE III

Results on BRIND with 1-pixel error tolerance without NMS:
The table is structured as in Table I, with results for the BRIND dataset.

	BRIND without NMS		
	ODS	OIS	AP
HED	0.645	0.656	0.417
HED-ES	0.668 (+3.57%)	0.677 (+3.20%)	0.466 (+11.75%)
HED-EES	0.679 (+5.27%)	0.687 (+4.73%)	0.492 (+17.98%)
HED-ES-U	0.668 (+3.57%)	0.673 (+2.59%)	0.522 (+25.18%)
HED-EES-U	0.669 (+3.72%)	0.676 (+3.05%)	0.543 (+30.22%)
BDCN	0.659	0.672	0.467
BDCN-ES	0.668 (+1.37%)	0.677 (+0.74%)	0.486 (+4.07%)
BDCN-EES	0.678 (+2.88%)	0.686 (+2.08%)	0.521 (+10.92%)
BDCN-ES-U	0.672 (+1.97%)	0.681 (+1.34%)	0.516 (+10.49%)
BDCN-EES-U	0.676 (+2.58%)	0.681 (+1.34%)	0.536 (+14.78%)
Dexi	0.666	0.672	0.478
Dexi-ES	0.671 (+0.75%)	0.678 (+0.89%)	0.485 (+1.46%)
Dexi-EES	0.683 (+2.55%)	0.691 (+2.83%)	0.490 (+2.51%)
Dexi-ES-U	0.666 (+0.00%)	0.673 (+0.15%)	0.529 (+10.04%)
Dexi-EES-U	0.662 (-0.60%)	0.669 (-0.45%)	0.521 (+9.00%)
A	0.657	0.667	0.454
A-ES	0.669 (+1.83%)	0.675 (+1.20%)	0.479 (+5.51%)
A-EES	0.680 (+3.50%)	0.688 (+3.15%)	0.501 (+10.35%)
A-ES-U	0.669 (+1.83%)	0.676 (+1.35%)	0.533 (+17.40%)
A-EES-U	0.669 (+1.83%)	0.675 (+1.20%)	0.533 (+17.40%)

namely the selector adopted in the main experimental setup.

- T2-Double: The same block setting as T2, but with doubled intermediate channel numbers of convolutional layers³.
- T3: Encoder blocks are also applied at $\frac{1}{4}$, besides $\frac{1}{8}$, and $\frac{1}{16}$ scales.
- T2U: Encoder blocks are moved to $\frac{1}{16}$ and $\frac{1}{8}$ in the up-sampling path, instead of the in the down-sampling path⁴.

The results show that selector architecture contributes marginal impact compared to introducing the E-S framework itself. While enlarging the selector (e.g., employing T2-Double instead of T2) yield modest gains, the standard selector works well. This confirms that the framework design, rather than the specific selector structure, is the dominant factor in performance improvement.

3) *Multiple Extractors and Multi-Level Selectors:* Table VI shows the effect of using multiple extractors and multiple levels of selection. Here, using multiple extractors represents that the extractors HED, BDCN, and Dexi are combined as a single multi-source extractor, while multi-level selection represents that the E-S or EES architecture is treated as a new extractor, with an additional selector applied on top. For example, 'Com-EES-L2' means applying one additional

³Namely, a convolutional layer outputting n channels is modified to output $2n$ channels, with the number of input channels of the next layer being modified accordingly. Note that this is not applied to the number of output channels in the first and last convolutional layers.

⁴Namely, encoder blocks are applied at the $\frac{1}{16}$ scale and the $\frac{1}{8}$ scale before up-sampling to the $\frac{1}{4}$ scale rather than before down-sampling to the $\frac{1}{16}$ scale.

TABLE IV

Standard E-S architecture with positional encoding in the selector: Results are on BRIND with 1-pixel error tolerance without NMS. Here, *Std* represents applying the standard positional encoding to all encoder blocks, *Rot* represents applying the rotary positional encoding to all encoder blocks, and *Once* represents applying the corresponding positional encoding only in the first encoder block per level rather than in all encoder blocks.

Benchmarks	Applying positional encoding in selectors		
	ODS	OIS	AP
HED-ES	0.668	0.677	0.466
Rot-HED-ES	0.671	0.680	0.474
Once-Rot-HED-ES	0.669	0.678	0.474
Std-HED-ES	0.668	0.677	0.463
Once-Std-HED-ES	0.668	0.677	0.479
HED-ES-U	0.668	0.673	0.522
Rot-HED-ES-U	0.665	0.672	0.532
Once-Rot-HED-ES-U	0.663	0.670	0.533
Std-HED-ES-U	0.667	0.674	0.526
Once-Std-HED-ES-U	0.662	0.669	0.533
BDCN-ES	0.668	0.677	0.486
Rot-BDCN-ES	0.668	0.676	0.481
Once-Rot-BDCN-ES	0.666	0.676	0.486
Std-BDCN-ES	0.668	0.676	0.479
Once-Std-BDCN-ES	0.667	0.676	0.484
BDCN-ES-U	0.672	0.681	0.516
Rot-BDCN-ES-U	0.652	0.660	0.510
Once-Rot-BDCN-ES-U	0.672	0.679	0.515
Std-BDCN-ES-U	0.656	0.664	0.511
Once-Std-BDCN-ES-U	0.679	0.688	0.504
Dexi-ES	0.671	0.678	0.485
Rot-Dexi-ES	0.671	0.677	0.492
Once-Rot-Dexi-ES	0.670	0.677	0.485
Std-Dexi-ES	0.671	0.677	0.490
Once-Std-Dexi-ES	0.670	0.677	0.482
Dexi-ES-U	0.666	0.673	0.529
Rot-Dexi-ES-U	0.668	0.674	0.510
Once-Rot-Dexi-ES-U	0.669	0.674	0.523
Std-Dexi-ES-U	0.669	0.675	0.519
Once-Std-Dexi-ES-U	0.667	0.673	0.512

selector on the normalized output features⁵ from the EES framework, while the extractor in such a situation is the one combining the three extractors⁶. The two fixed features, the zeros and the ones, are also being added to features of every level when employing high-level selections via the EES framework.

Results show that:

- In the standard E-S framework, using multiple extractors

⁵Namely, the features after multiplying weights but before summing, and are normalized by dividing by the maximum value, scaling to the [0,1] range.

⁶Namely, the concatenation of their outputted features are treated as the final outputted features.

TABLE V

The standard E-S architecture with different selector Structures: The results are on BRIND with 1-pixel error tolerance without NMS. The notations are the same as in the main-text.

Benchmarks	Different selector structures		
	ODS	OIS	AP
HED-T0-ES	0.668	0.677	0.465
HED-T1-ES	0.668	0.677	0.469
HED-T2-ES	0.668	0.677	0.466
HED-T2-Double-ES	0.673	0.682	0.483
HED-T2U-ES	0.669	0.679	0.475
HED-T3-ES	0.667	0.677	0.467
HED-T0-ES-U	0.662	0.670	0.526
HED-T1-ES-U	0.663	0.671	0.525
HED-T2-ES-U	0.668	0.673	0.522
HED-T2-Double-ES-U	0.662	0.670	0.536
HED-T2U-ES-U	0.666	0.672	0.529
HED-T3-ES-U	0.663	0.671	0.525
BDCN-T0-ES	0.666	0.676	0.481
BDCN-T1-ES	0.667	0.676	0.481
BDCN-T2-ES	0.668	0.677	0.486
BDCN-T2-Double-ES	0.669	0.678	0.492
BDCN-T2U-ES	0.667	0.676	0.477
BDCN-T3-ES	0.666	0.676	0.491
BDCN-T0-ES-U	0.671	0.678	0.503
BDCN-T1-ES-U	0.662	0.671	0.520
BDCN-T2-ES-U	0.672	0.681	0.516
BDCN-T2-Double-ES-U	0.674	0.682	0.518
BDCN-T2U-ES-U	0.667	0.676	0.516
BDCN-T3-ES-U	0.670	0.678	0.516
Dexi-T0-ES	0.670	0.677	0.485
Dexi-T1-ES	0.670	0.677	0.483
Dexi-T2-ES	0.671	0.678	0.485
Dexi-T2-Double-ES	0.673	0.680	0.493
Dexi-T2U-ES	0.671	0.677	0.482
Dexi-T3-ES	0.670	0.677	0.480
Dexi-T0-ES-U	0.668	0.674	0.511
Dexi-T1-ES-U	0.669	0.676	0.512
Dexi-T2-ES-U	0.666	0.673	0.529
Dexi-T2-Double-ES-U	0.669	0.676	0.533
Dexi-T2U-ES-U	0.667	0.674	0.509
Dexi-T3-ES-U	0.670	0.676	0.528

improves performance. This confirms that features from the standard extractor, namely the outputs of previous models, have been compressed with substantial details lost, and therefore employing multiple extractor scores benefits the final predictions since providing more features allows fewer details lost.

- In the EES framework, combining extractors shows only comparable results on ODS/OIS relative to the best single-extractor configuration. This confirms the effectiveness of employing richer and less-loss features as EES does. Namely, features employed in the EES framework are rich enough to provide sufficient options corresponding to the extractor for the selectors, making additional extractors less impactful, although whether the best scores can be obtained depends on whether the best extractor is employed.
- In both cases, employing higher-level selections only provides negative effects. This demonstrates that one-level selection is sufficient and more selection can lead to overfitting or diluted features.
- Double the network size of the selector still provides positive results.

Importantly, using multiple extractors does not degrade performance significantly, demonstrating the selector’s ability to prioritize useful features. Thus, when the best selection of the extractor is uncertain, combining several and deferring the choice to the selector can be a practical strategy.

TABLE VI

The proposed frameworks with multiple extractors and multiple-level selections: The results are on BRIND with 1-pixel error tolerance without NMS. Here, *Com* represents the result related to the combination of the three extractors, HED, BDCN, and Dexi, while *L1*, *L2*, *L3* represents applying the selector once, twice, and three times, respectively. For example, *Com-EES-L2* represents that the final extractor is a combination of the three extractors, and the selector is applied twice, under the EES framework.

	Multiple extractors and multi-level selectors		
	ODS	OIS	AP
HED-ES	0.668	0.677	0.466
BDCN-ES	0.668	0.677	0.486
Dexi-ES	0.671	0.678	0.485
Com-ES-L1-3	0.678	0.685	0.513
Com-ES-L2-3	0.670	0.681	0.403
HED-EES	0.679	0.687	0.492
BDCN-EES	0.678	0.686	0.521
Dexi-EES	0.683	0.691	0.490
Com-EES-L1	0.679	0.688	0.576
Com-EES-L2	0.676	0.688	0.560
Com-EES-L3	0.675	0.687	0.536
Com-EES-Double-L1	0.683	0.690	0.592
Com-EES-Double-L2	0.681	0.689	0.548

V. DISCUSSION

While this work is centered on edge detection, the E-S paradigm is broadly applicable across a wide range of vision tasks. Indeed, results on BSDS500 and NYUD2 datasets demonstrate that the framework could also be suitable for tasks like contour detection and segmentation, please refer to the supplementary materials. Many image-processing challenges benefit from pixel-level feature discrimination, due to the inherently heterogeneous nature of visual data—where structures like edges and textures, high-frequency and low-frequency patterns must be treated differently. Although the research community has extensively explored feature extractors, feature selection remains relatively underdeveloped. We hope this work provides a foundation for advancing this aspect of vision models, encouraging further exploration into robust, generalizable selector designs for a wider range of tasks.

Despite the promising results, several directions remain open for future research:

- **Specifically-designed Extractors:** While we have demonstrated improvements using existing extractors, designing dedicated extractors tailored for E-S or EES frameworks may yield even better performance.
- **Efficiency Improvements:** Enhancing the computational efficiency of the standard and enhanced architectures would increase their viability for real-time or resource-constrained applications, such as high-resolution edge detection in autonomous systems.
- **Balancing Quantitative and Perceptual Quality:** The best quantitative may be achieved without the union training stage, while the most perceptually appealing predictions may be obtained with it. Future work may focus on developing strategies that reconcile this trade-off, achieving both the best metrics and visual quality simultaneously.

VI. CONCLUSION

In this paper, we introduced a novel Extractor-Selector (E-S) paradigm to enhance image-processing tasks, with a particular focus on edge detection (ED). Unlike prior models that primarily rely on image-level feature fusion, our method emphasizes pixel-wise feature selection, allowing significantly improved performance.

To address the limitations of the standard E-S framework—specifically its insufficient exploitation of less-loss features—we further proposed the Enhanced Extractor-Selector (EES) framework. By leveraging richer, less-degraded intermediate feature representations and incorporating auxiliary features, the EES architecture delivers more quantitatively accurate and perpetually high-quality edge predictions.

Comprehensive experiments across multiple benchmark datasets demonstrate the substantial performance gains achieved by both the E-S and EES frameworks. Ablation studies further confirm that these improvements are primarily attributed to the framework itself, rather than the specific design of the selector module, highlighting the general utility and robustness of the proposed paradigm. Additionally, the high compatibility of our frameworks with existing models facilitates straightforward adoption and practical deployment,

making them a versatile and powerful enhancement strategy for ED systems, while the experimental results on contour detection and segmentation datasets indicate their potential to extend to broader image tasks.

In summary, the proposed E-S and EES frameworks offer a simple yet powerful paradigm that advances the state of edge detection and opens up promising pathways for broader applications in image processing and computer vision.

VII. BIBLIOGRAPHY

REFERENCES

- [1] K. Nazeri, E. Ng, T. Joseph, F. Qureshi, and M. Ebrahimi. Edgeconnect: Structure guided image inpainting using edge prediction. In *2019 IEEE/CVF International Conference on Computer Vision Workshop (ICCVW)*, pages 3265–3274, 2019.
- [2] C. H. Zhan, X. H. Duan, S. Y. Xu, Z. Song, and M. Luo. An improved moving object detection algorithm based on frame difference and edge detection. In *Fourth international conference on image and graphics (ICIG 2007)*, pages 519–523. IEEE, 2007.
- [3] R. Muthukrishnan and M. Radha. Edge detection techniques for image segmentation. *International Journal of Computer Science & Information Technology*, 3(6):259, 2011.
- [4] J. Kittler. On the accuracy of the sobel edge detector. *Image and Vision Computing*, 1(1):37–42, 1983.
- [5] J. Canny. A computational approach to edge detection. *IEEE Transactions on pattern analysis and machine intelligence*, PAMI-8(6):679–698, 1986.
- [6] S. Konishi, A. L. Yuille, J. M. Coughlan, and S. C. Zhu. Statistical edge detection: learning and evaluating edge cues. *IEEE Transactions on Pattern Analysis and Machine Intelligence*, 25(1):57–74, 2003.
- [7] P. Arbeláez, M. Maire, C. Fowlkes, and J. Malik. Contour detection and hierarchical image segmentation. *IEEE Transactions on Pattern Analysis and Machine Intelligence*, 33(5):898–916, 2011.
- [8] D.R. Martin, C.C. Fowlkes, and J. Malik. Learning to detect natural image boundaries using local brightness, color, and texture cues. *IEEE Transactions on Pattern Analysis and Machine Intelligence*, 26(5):530–549, 2004.
- [9] P. Dollar, Z. W. Tu, and S. Belongie. Supervised learning of edges and object boundaries. In *2006 IEEE Computer Society Conference on Computer Vision and Pattern Recognition (CVPR'06)*, volume 2, pages 1964–1971, 2006.
- [10] X. F. Ren. Multi-scale improves boundary detection in natural images. In *Computer Vision—ECCV 2008: 10th European Conference on Computer Vision, Marseille, France, October 12–18, 2008, Proceedings, Part III 10*, pages 533–545. Springer, 2008.
- [11] J. J. Lim, C. L. Zitnick, and P. Dollár. Sketch tokens: A learned mid-level representation for contour and object detection. In *Proceedings of the IEEE conference on computer vision and pattern recognition*, pages 3158–3165, 2013.

- [12] Y. Ganin and V. Lempitsky. n^4 -fields: neural network nearest neighbor fields for image transforms. In *Asian conference on computer vision*, pages 536–551. Springer, 2014.
- [13] P. Dollár and C. L. Zitnick. Fast edge detection using structured forests. *IEEE Transactions on Pattern Analysis and Machine Intelligence*, 37(8):1558–1570, 2015.
- [14] G. Bertasius, J. B. Shi, and L. Torresani. Deepedge: A multi-scale bifurcated deep network for top-down contour detection. In *Proceedings of the IEEE conference on computer vision and pattern recognition*, pages 4380–4389, 2015.
- [15] Y. Liu, M. M. Cheng, X. W. Hu, K. Wang, and X. Bai. Richer convolutional features for edge detection. In *Proceedings of the IEEE conference on computer vision and pattern recognition*, pages 3000–3009, 2017.
- [16] M. Le and S. Kayal. Revisiting edge detection in convolutional neural networks. In *2021 International Joint Conference on Neural Networks (IJCNN)*, pages 1–9. IEEE, 2021.
- [17] Z. Su, W. Z. Liu, Z. T. Yu, D. W. Hu, Q. Liao, Q. Tian, M. Pietikäinen, and L. Liu. Pixel difference networks for efficient edge detection. In *Proceedings of the IEEE/CVF international conference on computer vision*, pages 5117–5127, 2021.
- [18] S. N. Xie and Z. W. Tu. Holistically-nested edge detection. In *Proceedings of the IEEE international conference on computer vision*, pages 1395–1403, 2015.
- [19] J. Z. He, S. L. Zhang, M. Yang, Y. H. Shan, and T. J. Huang. Bdcn: Bi-directional cascade network for perceptual edge detection. *IEEE Transactions on Pattern Analysis and Machine Intelligence*, 44(1):100–113, 2022.
- [20] X. Soria, A. Sappa, P. Humanante, and A. Akbarinia. Dense extreme inception network for edge detection. *Pattern Recognition*, 139:109461, 2023.
- [21] M. Y. Pu, Y. P. Huang, Y. M. Liu, Q. J. Guan, and H. B. Ling. Edter: Edge detection with transformer. In *Proceedings of the IEEE/CVF conference on computer vision and pattern recognition*, pages 1402–1412, 2022.
- [22] J. H. Jie, Y. Guo, G. X. Wu, J. M. Wu, and B. J. Hua. Edgenat: Transformer for efficient edge detection. *arXiv preprint arXiv:2408.10527*, 2024.
- [23] C. x. Zhou, Y. P. Huang, M. C. Xiang, J. H. Ren, H. B. Ling, and J. Zhang. Generative edge detection with stable diffusion. *arXiv preprint arXiv:2410.03080*, 2024.
- [24] Y. F. Ye, K. Xu, Y. H. Huang, R. J. Yi, and Z. P. Cai. Diffusionedge: Diffusion probabilistic model for crisp edge detection. In *Proceedings of the AAAI conference on artificial intelligence*, volume 38, pages 6675–6683, 2024.
- [25] C. S. Liu, W. Zhang, Y. Y. Liu, M. Y. Li, W. L. Li, Y. M. Fan, X. N. Bai, and L. Zhang. Cycle pixel difference network for crisp edge detection. *Neurocomputing*, 619:129153, 2025.
- [26] D. Martin, C. Fowlkes, D. Tal, and J. Malik. A database of human segmented natural images and its application to evaluating segmentation algorithms and measuring ecological statistics. In *Proc. 8th Int'l Conf. Computer Vision*, volume 2, pages 416–423, July 2001.
- [27] D. A. Mély, J. k. Kim, M. McGill, Y. L. Guo, and T. Serre. A systematic comparison between visual cues for boundary detection. *Vision Research*, 120:93–107, 2016. *Vision and the Statistics of the Natural Environment*.
- [28] N. N. Silberman, D. Hoiem, P. P. Kohli, and R. Fergus. Indoor segmentation and support inference from rgb-d images. In *European Conference on Computer Vision*, 2012.
- [29] M. Everingham, L. Van Gool, C. K. I. Williams, J. Winn, and A. Zisserman. The pascal visual object classes (voc) challenge. *International Journal of Computer Vision*, 88(2):303–338, jun 2010.
- [30] T. Y. Lin, M. Maire, S. Belongie, L. Bourdev, R. Girshick, J. Hays, P. Perona, D. Ramanan, C. L. Zitnick, and P. Dollár. Microsoft coco: Common objects in context. In *Computer Vision – ECCV 2014*, pages 740–755. Springer International Publishing, 2014.
- [31] B. L. Zhou, H. Zhao, X. Puig, S. Fidler, A. Barriuso, and A. Torralba. Scene parsing through ade20k dataset. In *2017 IEEE Conference on Computer Vision and Pattern Recognition (CVPR)*, pages 5122–5130, 2017.
- [32] M. Cordts, M. Omran, S. Ramos, T. Rehfeld, M. Enzweiler, R. Benenson, U. Franke, S. Roth, and B. Schiele. The cityscapes dataset for semantic urban scene understanding. In *Proceedings of the IEEE Conference on Computer Vision and Pattern Recognition (CVPR)*, June 2016.
- [33] X. Soria, E. Riba, and A. Sappa. Dense extreme inception network: Towards a robust cnn model for edge detection. In *2020 IEEE Winter Conference on Applications of Computer Vision (WACV)*, pages 1912–1921. IEEE Computer Society, mar 2020.
- [34] M. Pu, Y. Huang, Q. Guan, and H. Ling. Rindnet: Edge detection for discontinuity in reflectance, illumination, normal and depth. In *2021 IEEE/CVF International Conference on Computer Vision (ICCV)*, pages 6859–6868. IEEE Computer Society, oct 2021.
- [35] X. Soria, Y. Li, M. Rouhani, and A. D. Sappa. Tiny and efficient model for the edge detection generalization. In *2023 IEEE/CVF International Conference on Computer Vision Workshops (ICCVW)*, pages 1356–1365. IEEE Computer Society, oct 2023.
- [36] Y. B. Fu and X. J. Guo. Practical edge detection via robust collaborative learning. In *Proceedings of the 31st ACM International Conference on Multimedia*, MM '23, page 2526–2534. Association for Computing Machinery, 2023.
- [37] C. Wang, D. Dai, S. Xia, Y. Liu, and G. Wang. One-stage deep edge detection based on dense-scale feature fusion and pixel-level imbalance learning. *IEEE Transactions on Artificial Intelligence*, 5(01):70–79, jan 2024.
- [38] Hao Shu. More precise edge detections. 2025.
- [39] R. X. Deng, C. H. Shen, S. J. Liu, H. B. Wang, and X. R. Liu. Learning to predict crisp boundaries. In *Computer Vision – ECCV 2018: 15th European Conference, Munich, Germany, September 8–14, 2018, Proceedings*,

- Part VI, page 570–586. Springer-Verlag, 2018.
- [40] L. X. Huan, N. Xue, X. W. Zheng, W. He, J. Y. Gong, and G. S. Xia. Unmixing convolutional features for crisp edge detection. *IEEE Trans. Pattern Anal. Mach. Intell.*, 44(10 Part 1):6602–6609, oct 2022.
- [41] K. Chen, J. G. Li, W. Y. Lin, J. See, J. Wang, L. Y. Duan, Z. B. Chen, C. W. He, and J. N. Zou. Towards accurate one-stage object detection with ap-loss. In *Proceedings of the IEEE/CVF Conference on Computer Vision and Pattern Recognition*, pages 5119–5127, 2019.
- [42] B. Cetinkaya, S. Kalkan, and E. Akbas. Ranked: Addressing imbalance and uncertainty in edge detection using ranking-based losses. In *Proceedings of the IEEE/CVF Conference on Computer Vision and Pattern Recognition*, pages 3239–3249, 2024.
- [43] A. Vaswani, N. Shazeer, N. Parmar, J. Uszkoreit, L. Jones, A. N. Gomez, L. Kaiser, and I. Polosukhin. Attention is all you need. In *Advances in Neural Information Processing Systems*, volume 30. Curran Associates, Inc., 2017.
- [44] A. Dosovitskiy. An image is worth 16x16 words: Transformers for image recognition at scale. *arXiv preprint arXiv:2010.11929*, 2020.
- [45] N. Carion, F. Massa, G. Synnaeve, N. Usunier, A. Kirillov, and S. Zagoruyko. End-to-end object detection with transformers. In *European conference on computer vision*, pages 213–229. Springer, 2020.
- [46] S. X. Zheng, J. C. Lu, H. S. Zhao, X. T. Zhu, Z. K. Luo, Y. B. Wang, Y. W. Fu, J. F. Feng, T. Xiang, P. H. S. Torr, and L. Zhang. Rethinking semantic segmentation from a sequence-to-sequence perspective with transformers. In *Proceedings of the IEEE/CVF conference on computer vision and pattern recognition*, pages 6881–6890, 2021.
- [47] X. Zhang, Y. L. Zhang, and F. Yu. Hit-sr: Hierarchical transformer for efficient image super-resolution. In *European Conference on Computer Vision*, pages 483–500. Springer, 2025.
- [48] J. L. Su, M. Ahmed, Y. Lu, S. F. Pan, W. Bo, and Y. F. Liu. Roformer: Enhanced transformer with rotary position embedding. *Neurocomputing*, 568:127063, 2024.

VIII. SUPPLEMENTARY MATERIALS

Supplementary experiment results are presented here, as well as the full details of the selector structure.

A. Results on BSDS500 and NYUD2

Table VII and VIII show the experiment results on BSDS500 and NYUD2 datasets.

B. Evaluation Results Under traditional relaxed settings

Table IX,X,XI,XII,XIII display the evaluation result under traditional relaxed settings, namely 0.0075 error tolerance set in the algorithm presented in [8] and with NMS. The setting results in error tolerances about 11.1 pixels for BIPED2, 4.3 pixels for BRIND and BSDS500, and 6 pixels for NYUD2, respectively.

TABLE VII

Results on BSDS500 Label 1, with 1-pixel error tolerance, without NMS: The table is structured as in Table I, with results for the BSDS500 dataset. In the experiment, only Label 1 of each image is employed as the ground-truth. The dataset is split into 400 training images and 100 testing images, with all training and assessing schemes following the main-text.

	BSDS500 Label 1 without NMS		
	ODS	OIS	AP
HED	0.420	0.433	0.175
HED-ES	0.466	0.479	0.253
HED-EES	0.492	0.504	0.261
HED-ES-U	0.459	0.471	0.272
HED-EES-U	0.484	0.493	0.305
BDCN	0.454	0.465	0.240
BDCN-ES	0.457	0.469	0.253
BDCN-EES	0.480	0.494	0.266
BDCN-ES-U	0.456	0.464	0.258
BDCN-EES-U	0.471	0.483	0.288
Dexi	0.465	0.473	0.242
Dexi-ES	0.467	0.475	0.249
Dexi-EES	0.487	0.501	0.261
Dexi-ES-U	0.473	0.484	0.271
Dexi-EES-U	0.472	0.485	0.277

TABLE VIII

Results on NYU2C, with 1-pixel error tolerance, without NMS: The table is structured as in Table I, with results for the NYUD2 dataset. The edge label (ground-truth) of each image is extracted by using the Canny operator from the segmentation label. The dataset is split into 1100 training images and 300 testing images, from the 1449 annotated data, with all training and assessing schemes following the main-text.

	NYU2C without NMS		
	ODS	OIS	AP
HED	0.376	0.386	0.146
HED-ES	0.396	0.406	0.158
HED-EES	0.409	0.418	0.154
HED-ES-U	0.402	0.411	0.172
HED-EES-U	0.410	0.418	0.171
BDCN	0.406	0.414	0.183
BDCN-ES	0.403	0.411	0.175
BDCN-EES	0.408	0.417	0.142
BDCN-ES-U	0.398	0.408	0.166
BDCN-EES-U	0.403	0.412	0.169
Dexi	0.408	0.416	0.161
Dexi-ES	0.406	0.414	0.160
Dexi-EES	0.402	0.413	0.158
Dexi-ES-U	0.414	0.422	0.181
Dexi-EES-U	0.417	0.427	0.174

TABLE IX

Results on BIPED2 with 11.1-pixel error tolerance, with NMS: The table is structured as in Table I. These are the results under the traditional evaluation settings that the error tolerance distance in the evaluation algorithm is set to 0.0075.

	BIPED2 with NMS		
	ODS	OIS	AP
HED	0.883	0.894	0.914
HED-ES	0.878	0.889	0.926
HED-EES	0.882	0.893	0.927
HED-ES-U	0.878	0.890	0.908
HED-EES-U	0.884	0.892	0.900
BDCN	0.880	0.891	0.912
BDCN-ES	0.879	0.890	0.918
BDCN-EES	0.881	0.890	0.921
BDCN-ES-U	0.876	0.886	0.922
BDCN-EES-U	0.884	0.891	0.860
Dexi	0.890	0.897	0.923
Dexi-ES	0.889	0.897	0.928
Dexi-EES	0.887	0.895	0.934
Dexi-ES-U	0.887	0.895	0.898
Dexi-EES-U	0.881	0.890	0.887

TABLE XI

Results on BRIND with 4.3-pixel error tolerance, with NMS: The table is structured as in Table I. These are the results under the traditional evaluation settings that the error tolerance distance in the evaluation algorithm is set to 0.0075.

	BRIND with NMS		
	ODS	OIS	AP
HED	0.784	0.799	0.832
HED-ES	0.787	0.800	0.843
HED-EES	0.789	0.803	0.849
HED-ES-U	0.785	0.796	0.799
HED-EES-U	0.788	0.801	0.806
BDCN	0.775	0.791	0.806
BDCN-ES	0.781	0.795	0.832
BDCN-EES	0.790	0.806	0.831
BDCN-ES-U	0.786	0.799	0.828
BDCN-EES-U	0.788	0.798	0.820
Dexi	0.794	0.809	0.828
Dexi-ES	0.792	0.806	0.837
Dexi-EES	0.792	0.806	0.842
Dexi-ES-U	0.789	0.803	0.795
Dexi-EES-U	0.783	0.796	0.794

TABLE X

Results on UDED with 0.0075 error tolerance, with NMS. The table is structured as in Table I. These are the results under the traditional evaluation settings that the error tolerance distance in the evaluation algorithm is set to 0.0075.

	UDED with NMS		
	ODS	OIS	AP
HED	0.819	0.857	0.806
HED-ES	0.820	0.852	0.823
HED-EES	0.823	0.845	0.856
HED-ES-U	0.794	0.829	0.799
HED-EES-U	0.833	0.861	0.802
BDCN	0.798	0.837	0.796
BDCN-ES	0.809	0.843	0.812
BDCN-EES	0.825	0.854	0.822
BDCN-ES-U	0.834	0.858	0.790
BDCN-EES-U	0.841	0.859	0.852
Dexi	0.829	0.858	0.824
Dexi-ES	0.829	0.859	0.829
Dexi-EES	0.852	0.869	0.889
Dexi-ES-U	0.847	0.865	0.793
Dexi-EES-U	0.853	0.874	0.767

TABLE XII

Results on BSDS500 Label 1, with 4.3-pixel error tolerance, with NMS: The table is structured as in Table I. These are the results under the traditional evaluation settings that the error tolerance distance in the evaluation algorithm is set to 0.0075.

	BSDS500 Label 1 with NMS		
	ODS	OIS	AP
HED	0.622	0.650	0.578
HED-ES	0.628	0.654	0.611
HED-EES	0.651	0.674	0.661
HED-ES-U	0.625	0.649	0.564
HED-EES-U	0.647	0.671	0.618
BDCN	0.628	0.650	0.596
BDCN-ES	0.628	0.649	0.602
BDCN-EES	0.640	0.666	0.641
BDCN-ES-U	0.617	0.640	0.570
BDCN-EES-U	0.636	0.659	0.601
Dexi	0.648	0.672	0.608
Dexi-ES	0.647	0.671	0.626
Dexi-EES	0.649	0.676	0.654
Dexi-ES-U	0.646	0.678	0.596
Dexi-EES-U	0.642	0.674	0.608

TABLE XIII**Results on NYU2C, with 6-pixel error tolerance, with NMS:**

The table is structured as in Table I. These are the results under the traditional evaluation settings that the error tolerance distance in the evaluation algorithm is set to 0.0075.

	NYU2C with NMS		
	ODS	OIS	AP
HED	0.703	0.716	0.694
HED-ES	0.712	0.724	0.712
HED-EES	0.710	0.721	0.687
HED-ES-U	0.715	0.725	0.674
HED-EES-U	0.723	0.733	0.682
BDCN	0.711	0.723	0.712
BDCN-ES	0.711	0.723	0.713
BDCN-EES	0.720	0.732	0.708
BDCN-ES-U	0.715	0.725	0.678
BDCN-EES-U	0.718	0.728	0.684
Dexi	0.715	0.725	0.728
Dexi-ES	0.714	0.724	0.723
Dexi-EES	0.634	0.644	0.652
Dexi-ES-U	0.725	0.735	0.685
Dexi-EES-U	0.728	0.738	0.688

C. Results on RCF

Since RCF can be viewed as an extended version of HED by employing richer features from different layers of the same scales, using it as the extractor on the EES framework is not valid since the EES framework of HED has already employed richer features. Here, we only display the experimental results with the standard E-S framework, please see Table XIV and XV. The E-S framework obtains the best results for most cases, especially under the suggested strict 1-pixel error tolerance.

D. Experiments of Positional Encoding of EES

Table XVI exhibits the performance of the EES architecture with various positional encoding strategies applied to the selector. Also, applying positional encoding provides no benefits mostly.

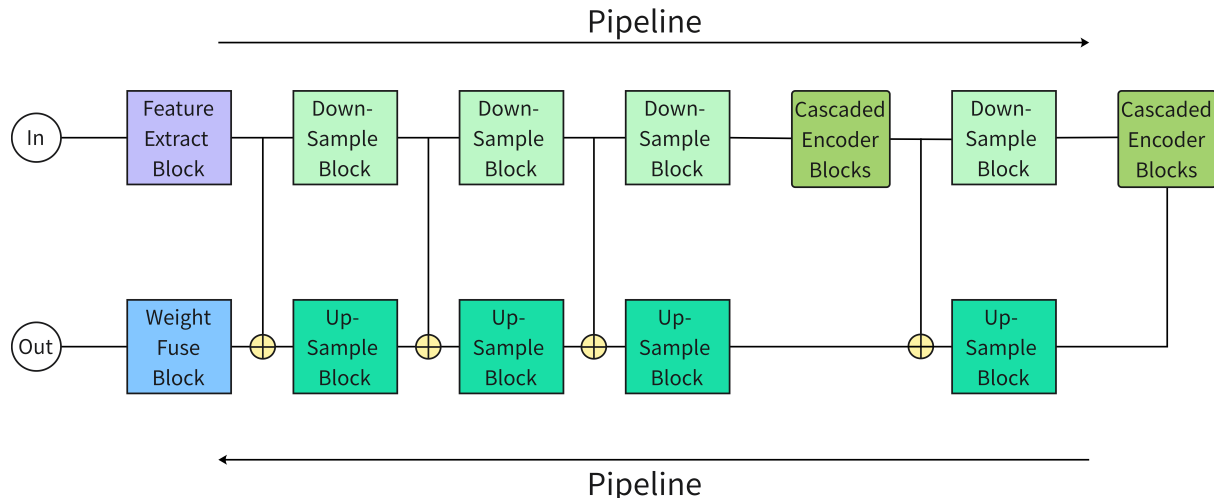
E. Detailed Descriptions of the Selector

The details of the blocks employed in the selector are displayed in Figure 6

TABLE XIV**Results on RCF, with 1-pixel error tolerance, without NMS:**

The table is structured as in Table I.

	RCF on BIPED2 without NMS		
	ODS	OIS	AP
RCF	0.591	0.597	0.345
RCF-S	0.641	0.645	0.418
RCF-S-U	0.666	0.672	0.502
RCF on UDED without NMS			
	ODS	OIS	AP
RCF	0.699	0.741	0.450
RCF-S	0.723	0.761	0.562
RCF-S-U	0.752	0.781	0.635
RCF on BRIND without NMS			
	ODS	OIS	AP
RCF	0.646	0.656	0.394
RCF-ES	0.667	0.675	0.475
RCF-ES-U	0.666	0.672	0.517
RCF on BSDS500 Label 1 without NMS			
	ODS	OIS	AP
RCF	0.426	0.441	0.190
RCF-S	0.459	0.472	0.239
RCF-S-U	0.461	0.474	0.274
RCF on NYUD2 without NMS			
	ODS	OIS	AP
RCF	0.374	0.382	0.149
RCF-S	0.392	0.400	0.154
RCF-S-U	0.398	0.407	0.157



(a) An overview architecture of the feature selector

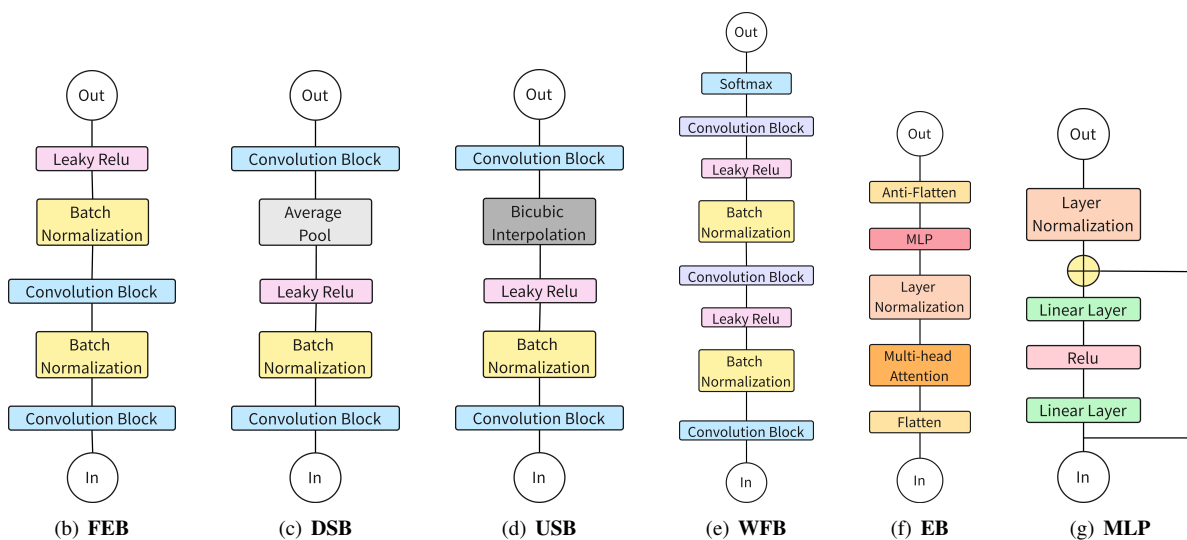
**Fig. 6** The architecture of the feature selector.

Figure 6(a) provides an overview of the feature selector. It is structured like a U-Net. The input images pass through a feature extraction block, followed by four $\frac{1}{2}$ down-sampling blocks to capture multi-scale features. At the $\frac{1}{8}$ and $\frac{1}{16}$ scales, cascaded transformer encoder blocks are applied. The features from the $\frac{1}{16}$ scale are progressively up-sampled, and each up-sample block incorporates a residual connection with a learnable coefficient to balance the up-sampled features and the features from the residual connections. Finally, pixel-wise weights are produced by fusing the ordinary-scale features.

Figure 6(b) (FEB) is the **Feature Extract Block**. It consists of two convolution layers, each followed by a batch normalization layer, and an activation function using Leaky ReLU. The convolution layers are 3×3 in size with each outputs 32 channels typically.

Figure 6(c) (DSB) is the **Down-Sample Block**. The down-sample operation applies a 3×3 average-pool operation with a stride of 2. The input features go through a 3×3 convolution layer that doubles the number of channels, followed by batch normalization, Leaky ReLU activation, and average pooling. Another convolution layer maintaining the number of input and output channels is then applied.

Figure 6(d) (USB) is the **Up-Sample Block**. It replaces the average-pool operation from the down-sample block with a $\times 2$ bi-cubic interpolation operation. The remaining structure is similar to the down-sample block. The convolution layers are also 3×3 in size, but the first one maintains the number of channels of the input and output while the second one halves the number of channels.

Figure 6(e) (WFB) is the final **Weight Fusing Block**. It includes a 3×3 convolution, batch normalization, and Leaky ReLU activation as the first group. A second structure is similar but with the 1×1 convolution instead of a 3×3 one. Finally, another 1×1 convolution is applied, followed by the Softmax function to produce pixel-wise weights. Typically, the number of output channels of the three convolutional layers is 64, 128, and the required number of output channels of the selector, respectively.

Figure 6(f) (EB) is the **Encoder Block** from transformers. It includes a flattening operation, a multi-head attention layer, layer normalization, and an MLP. The flattening operation transforms 2D images into 1D vectors for processing in the multi-head attention layer, which typically uses 8 attention heads. The MLP further processes the features, and the resulting features are then reshaped back into 2D images.

Figure 6(g) (MLP) is the Multiple Layer Perception (MLP). It consists of two linear layers with ReLU activation, a residual connection, and layer normalization. The numbers of input and output states are the same, while the number of middle states is four times as it.

TABLE XV

Results on RCF, with 0.0075 error tolerance, with NMS: The table is structured as in Table I.

RCF on BIPED2 with NMS			
	ODS	OIS	AP
RCF	0.887	0.895	0.914
RCF-ES	0.882	0.891	0.927
RCF-ES-U	0.881	0.890	0.901
RCF on UDED with NMS			
	ODS	OIS	AP
RCF	0.794	0.843	0.775
RCF-ES	0.799	0.845	0.833
RCF-ES-U	0.825	0.852	0.805
RCF on BRIND with NMS			
	ODS	OIS	AP
RCF	0.786	0.800	0.836
RCF-ES	0.785	0.797	0.839
RCF-ES-U	0.783	0.793	0.796
RCF on BSDS500 Label 1 with NMS			
	ODS	OIS	AP
RCF	0.624	0.655	0.575
RCF-ES	0.626	0.655	0.595
RCF-ES-U	0.629	0.651	0.558
RCF on NYUD2 with NMS			
	ODS	OIS	AP
RCF	0.702	0.714	0.660
RCF-ES	0.712	0.724	0.679
RCF-ES-U	0.719	0.728	0.673

TABLE XVI

EES architecture with positional encoding in the selector: Results are on BRIND with 1-pixel error tolerance without NMS. The notations are the same as in the main-text.

Benchmarks	Applying positional encoding in selectors		
	ODS	OIS	AP
HED-EES	0.679	0.687	0.492
Rot-HED-EES	0.679	0.689	0.517
Once-Rot-HED-EES	0.636	0.646	0.435
Std-HED-EES	0.678	0.685	0.522
Once-Std-HED-EES	0.674	0.684	0.508
HED-EES-U	0.668	0.673	0.522
Rot-HED-EES-U	0.667	0.675	0.539
Once-Rot-HED-EES-U	0.665	0.673	0.529
Std-HED-EES-U	0.664	0.671	0.530
Once-Std-HED-EES-U	0.668	0.675	0.504
BDCN-EES	0.678	0.686	0.521
Rot-BDCN-EES	0.677	0.686	0.519
Once-Rot-BDCN-EES	0.678	0.687	0.503
Std-BDCN-EES	0.678	0.686	0.516
Once-Std-BDCN-EES	0.678	0.687	0.513
BDCN-EES-U	0.672	0.681	0.516
Rot-BDCN-EES-U	0.672	0.680	0.535
Once-Rot-BDCN-EES-U	0.660	0.667	0.507
Std-BDCN-EES-U	0.656	0.662	0.502
Once-Std-BDCN-EES-U	0.667	0.675	0.486
Dexi-EES	0.683	0.691	0.490
Rot-Dexi-EES	0.647	0.658	0.424
Once-Rot-Dexi-EES	0.644	0.654	0.433
Std-Dexi-EES	0.682	0.690	0.479
Once-Std-Dexi-EES	0.680	0.688	0.496
Dexi-EES-U	0.666	0.673	0.529
Rot-Dexi-EES-U	0.666	0.672	0.517
Once-Rot-Dexi-EES-U	0.664	0.672	0.526
Std-Dexi-EES-U	0.664	0.672	0.522
Once-Std-Dexi-EES-U	0.657	0.664	0.506